Journal of Materials Chemistry A

ROYAL SOCIETY OF CHEMISTRY

PAPER

View Article Online
View Journal | View Issue

Cite this: J. Mater. Chem. A, 2023, 11, 5309

Transition metal hydroxides@conducting MOFs on carbon nanotube yarns for ultra-stable quasi-solid-state supercapacitors with a ship-in-a-bottle architecture†

Qingli Xu,[a] Xia Liu,[b] Juan Zhang,[a] Yifei Xu,[c] Mi Zhou,[d] Jiaxin Li,[c] Minzhi Du,[a] Kun Zhang,[c] Xiangyu Qian,[a] Bo Xu,[d] Xinhou Wang,[a] Bingjie Wang *[c] and Kun Zhang *[a]

Yarn-shaped supercapacitors (SCs) functionalized with pseudocapacitive materials show promise in wearable electronics. However, their development was hindered by poor electrochemical properties, especially long-term cycling stability, owing to the volumetric change during charging/discharging. Herein, we report a ship-in-a-bottle architecture on carbon nanotube yarn (CNTY) based SCs, in which transition metal hydroxide (TMH) nanoparticles ($Ni(OH)_2$ or $Co(OH)_2$) are confined in conducting nanoporous metal–organic frameworks (MOFs, $Ni_3(HITP)_2$) which anchor onto CNTY, involves the synergy of nanoconfinement and hydrogen bonding (H-bonding) network to mutually support each phase toward improved electrochemical performance. The $Ni(OH)_2$@$Ni_3(HITP)_2$@CNTY electrode possesses an areal specific capacitance of 496 mF cm^{-2} at 0.4 mA cm^{-2} due to the hierarchical structure which led to facilitated charge transport and enhanced ion storage. Moreover, the ternary CNTY-based SCs demonstrate exceptional cycle performance (90.9–92.3% capacitance retention after 10 000 cycles at 5 mA cm^{-2}). Importantly, the nanoconfinement is confirmed by field emission scanning electron microscopy, transmission electron microscopy-energy dispersive spectroscopy, and energy dispersive spectroscopy, and Brunauer–Emmett–Teller and cryogenic-TEM characterization studies. The H-bonding (O···H–N) network between $Ni(OH)_2$ and $Ni_3(HITP)_2$ is confirmed by Fourier transform infrared spectroscopy and density functional theory calculations. Both nanoconfinement and the H-bonding network contribute to an ultra-stable $Ni(OH)_2$@$Ni_3(HITP)_2$ structure due to its high durability to volumetric change caused by phase separation and structural collapse during charging/discharging.

Received 6th October 2022
Accepted 30th January 2023

DOI: 10.1039/d2ta07804j

rsc.li/materials-a

1. Introduction

Yarn-shaped supercapacitors (SCs) are promising for the next-generation wearable electronics due to their high power density, rapid charge process, tiny volume, high flexibility and weavability.[1,2] Carbon nanotube yarn (CNTY) are considered as one of the most promising flexible yarn-based electrodes due to its excellent flexibility and weavability as well as superior electrical and mechanical properties.[3–7] However, the pristine CNTY usually suffers from low specific capacitance and energy density due to the limited energy storage in the assembled electric double layer capacitive devices.[8–10]

Pseudocapacitive materials, *i.e.*, conducting polymers (CPs) and transition metal oxides/hydroxides (TMOs/TMHs), are usually used to functionalize CNTY to improve specific capacitance.[11,12] In general, TMOs/TMHs can provide higher theoretical specific capacitance and better electrochemical stability than conducting polymers.[13] However, the charge transport and cyclic stability of CNTY hybridized with TMOs (TMO@CNTY) or TMHs (TMH@CNTY) are unsatisfactory (Generally, the capacitance retention of TMO@CNTY or TMH@CNTY is 65–85% after 1000–10 000 cycles) because of the poor structural stability as well as the ultralow electrical conductivity (10^{-5} to 10^{-6} S cm^{-1}).[14] The structural collapse of TMOs/TMHs originates from the swelling/shrinkage during repeated charging/discharging, thus lowering the cyclic life dramatically.[15] Moreover, the

[a]Key Laboratory of Textile Science & Technology of Ministry of Education, College of Textiles, Donghua University, 2999 North Renmin Road, Shanghai 201620, P.R. China. E-mail: kun.zhang@dhu.edu.cn

[b]State Key Laboratory of Chemo/Biosensing and Chemometrics, Hunan University, Changsha 410082, China

[c]Laboratory of Advanced Materials, State Key Laboratory of Molecular Engineering of Polymers, Department of Macromolecular Science, Fudan University, 2205 Songhu Road, Shanghai 200438, P.R. China. E-mail: wangbingjie@fudan.edu.cn

[d]College of Chemistry, Chemical Engineering and Biotechnology, Donghua University, 2999 North Renmin Road, Shanghai 201620, P.R. China

† Electronic supplementary information (ESI) available. See DOI: https://doi.org/10.1039/d2ta07804j

weak interaction between TMOs/TMHs and CNTs makes TMO/TMH nanoparticles (NPs) easily peel off from CNTY during charging/discharging, especially at a high current density, which further deteriorates the durability and rate capability.[14,16]

Recently, conducting two-dimensional metal–organic frameworks (MOFs) have been considered as prevalent candidates for SCs owing to their high porosity, high specific surface area, high electrical conductivity and versatile functionalities.[17–19] However, conducting MOFs with high porosity tend to degrade and collapse as a result of the adsorption/desorption of solvated electrolyte ions during charging/discharging. It typically occurs during the removal of strongly associated solvent molecules (*i.e.,* water) in their pores due to capillary force.[20–22] Moreover, MOFs are vulnerable in acidic and basic electrolytes which can destroy metal coordination.[23]

In this study, we adopt a facile but robust ship-in-a-bottle structure to obtain exceptional electrochemical performance with enhanced kinetics and stability by growing TMHs ($Ni(OH)_2$ or $Co(OH)_2$) into the nanopores of conducting MOFs (Ni_3(2,3,6,7,10,11-hexaiminotriphenylene)$_2$, $Ni_3(HITP)_2$) which are *in situ* anchored onto CNTYs by π–π interaction in advance. The physical nanoconfinement and hydrogen bonding (H-bonding) between TMH NPs and $Ni_3(HITP)_2$ can interlock each other to avoid structure collapse of TMHs NPs@$Ni_3(HITP)_2$ with limited swelling/shrinking during charging/discharging. Hence, both $Ni_3(HITP)_2$ and TMH NPs mutually work as a structure support and ion buffer to synergistically enable the ternary electrodes with enhanced electrochemical properties and an ultra-stable structure. The $Ni(OH)_2$@$Ni_3(HITP)_2$@CNTY electrode shows an areal specific capacitance as high as 496.0 mF cm^{-2} at 0.4 mA cm^{-2}, leading to an energy density of 49.8 μW h cm^{-2} at a power density of 340.0 μW cm^{-2}. Moreover, the ternary-based SCs exhibit high cycle stability of 90.9–92.3% capacitance retention at 5 mA cm^{-2} after 10 000 cycles.

2. Results and discussion

2.1 Ship-in-a-bottle structure of TMH NPs@$Ni_3(HITP)_2$@CNTYs

The typical binary and ternary CNTY-based electrodes (TMH NPs@$Ni_3(HITP)_2$@CNTYs with a ship-in-a-bottle structure) were synthesized by a hydrothermal/vapor phase method (Fig. 1a and ESI Fig. 1†). As compared to pristine CNTs (ESI Fig. 2†), $Ni(OH)_2$ NPs coated CNTs ($Ni(OH)_2$@CNT, Fig. 1b, c and j) show a rough surface with a coating thickness of ~2.7 nm. Compared to $Ni_3(HITP)_2$@$CNT_{(2)}$ (two-day synthesis, ESI Fig. 3a†) and $Ni_3(HITP)_2$@$CNT_{(4)}$ (four-day synthesis, ESI Fig. 3b†), the $Ni_3(HITP)_2$ (one-day synthesis, Fig. 1d) coating on CNTs ($Ni_3(HITP)_2$@CNT) possesses a rough but uniform core–shell structure with a total diameter of ~20 nm (ESI Fig. 4†). The thickness of $Ni_3(HITP)_2$ nanolayer (Fig. 1e) is ~4 nm, corresponding to ~13 atomic layers of $Ni_3(HITP)_2$, which can form a one-dimensional channel by slipped-parallel stacking among adjacent layers. The $Ni_3(HITP)_2$ nanolayer on CNTs displays no lattice structure (Fig. 1k), probably due to structural decomposition under high-energy electron beam irradiation.[24,25] Moreover, the element mapping patterns of $Ni_3(HITP)_2$@CNT (ESI Fig. 5†) show that N and Ni elements from $Ni_3(HITP)_2$ are evenly distributed on the CNT surface, which further confirms the *in situ* growth of the $Ni_3(HITP)_2$ layer on CNTs.

After the incorporation of $Ni(OH)_2$ NPs into $Ni_3(HITP)_2$, $Ni(OH)_2$@$Ni_3(HITP)_2$@CNT (Fig. 1f) shows similar to but rougher morphology than $Ni_3(HITP)_2$@CNT. Its average diameter (~21 nm, ESI Fig. 4†) is comparable to that of $Ni_3(HITP)_2$@CNT (~20 nm), indicating subtle change in the coating thickness after incorporation of $Ni(OH)_2$ NPs into the nanopores of $Ni_3(HITP)_2$, which has been further confirmed by cryogenic-TEM (cryo-TEM) characterization (Fig. 3c–h). Additionally, the mass loadings of $Ni_3(HITP)_2$ and $Ni(OH)_2$ NPs in $Ni(OH)_2$@$Ni_3(HITP)_2$@CNTY (ESI Fig. 6†) were calculated to be 0.16 mg cm^{-2} (13.6 wt%) and 0.10 mg cm^{-2} (8.4 wt%), respectively. Fig. 1g shows the absent inner cavity of CNTs, indicating the high-density matter covering on the surface of CNTs. The lattice with $d = 0.27$ nm corresponds well to the (100) plane of $Ni(OH)_2$ (Fig. 1l).[26] Element mapping patterns in ESI Fig. 7† showing C, N, O and Ni elements distribution suggest that $Ni(OH)_2$ NPs are evenly distributed on the surface of CNTs. Moreover, the Brunauer–Emmett–Teller (BET)-based specific surface area of $Ni(OH)_2$@$Ni_3(HITP)_2$@CNT (136.4 m^2 g^{-1}) is higher than that of $Ni(OH)_2$@CNT (94.4 m^2 g^{-1}) but lower than that of $Ni_3(HITP)_2$@CNT (159.6 m^2 g^{-1}) and CNTs (167.2 m^2 g^{-1}), which is attributed to the incorporation of $Ni(OH)_2$ NPs in the nanopores of $Ni_3(HITP)_2$ and the larger coating-induced diameter of CNTs (ESI Fig. 8a†). In the pore size distributions, the pores with a diameter of ~1.6 nm in $Ni_3(HITP)_2$@CNT must have originated from $Ni_3(HITP)_2$, since the pores with an average diameter of ~1.4 nm come from CNTs, suggesting that $Ni_3(HITP)_2$ on CNTs displays good nano-architecture for $Ni(OH)_2$ NPs (ESI Fig. 8b†). Furthermore, the incremental pore volume of pores at ~1.6 nm in $Ni(OH)_2$@$Ni_3(HITP)_2$@CNT is 3.4 mm^3 g^{-1}, which is smaller than that in $Ni_3(HITP)_2$@CNT (4.2 mm^3 g^{-1}) (ESI Fig. S8c and d†), further suggesting the incorporation of $Ni(OH)_2$ NPs inside $Ni_3(HITP)_2$.

Moreover, $Co(OH)_2$@$Ni_3(HITP)_2$@CNTY and $Co(OH)_2$@$Ni_3(HITP)_2$ were also prepared to clearly testify the target hierarchical structure, since both $Ni(OH)_2$ and the ligand in $Ni_3(HITP)_2$ have Ni element. The morphology of $Co(OH)_2$@$Ni_3(HITP)_2$@CNT (Fig. 1h and i) is very similar to that of $Ni(OH)_2$@$Ni_3(HITP)_2$@CNT. Moreover, the lattice on $Co(OH)_2$@$Ni_3(HITP)_2$@CNT with $d = 0.46$ nm corresponds to the (002) plane of $Co(OH)_2$ (Fig. 1m), which indicates the existence of $Co(OH)_2$.[27] Besides, the specific surface area of $Co(OH)_2$@$Ni_3(HITP)_2$@CNT is 103.2 m^2 g^{-1}, and the incremental pore volume at ~1.6 nm sharply goes down, suggesting $Co(OH)_2$ NPs are confined in $Ni_3(HITP)_2$, which further confirms that $Ni_3(HITP)_2$ can work as a platform to confine NPs (ESI Fig. 8c and d†).

We further employed cryo-TEM characterization for the active hybrid material ($Co(OH)_2$@$Ni_3(HITP)_2$) to confirm the successful filling of $Co(OH)_2$ NPs in the pores of $Ni_3(HITP)_2$. In addition, $Co(OH)_2$@$Ni_3(HITP)_2$ was selected for characterization instead of $Co(OH)_2$@$Ni_3(HITP)_2$@CNT to eliminate the influence of the electron diffraction signal from CNTs. The bright-field cryo-TEM characterization enables high-resolution imaging of delicate MOF-based samples by operating under cryogenic conditions to

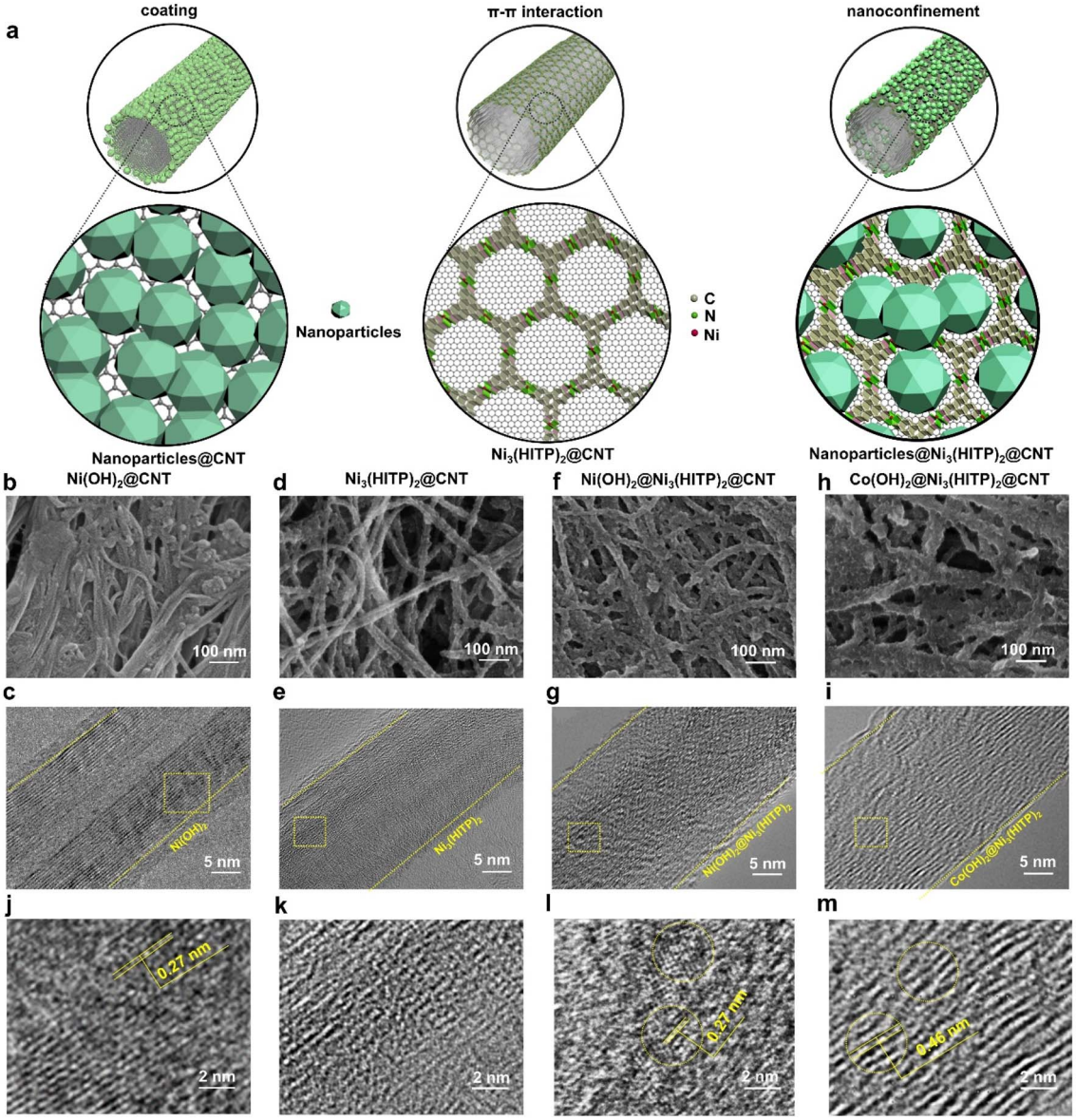

Fig. 1 (a) Schematic illustration of hybridized CNT architectures. From left to right: NPs are directly coated on CNTs to form NPs@CNT; Ni_3(-HITP)$_2$ is stably coated on CNTs by strong π−π interaction to form $Ni_3(HITP)_2$@CNT; NPs are confined in the nanopores of $Ni_3(HITP)_2$ to obtain NPs@$Ni_3(HITP)_2$@CNT. FESEM images, TEM images and corresponding selected high resolution TEM images of (b, c and j) $Ni(OH)_2$@CNT, (d, e and k) $Ni_3(HITP)_2$@CNT, (f, g and l) $Ni(OH)_2$@$Ni_3(HITP)_2$@CNT, and (h, i and m) $Co(OH)_2$@$Ni_3(HITP)_2$@CNT.

minimize the electron beam damage. Compared to the cryo-TEM images of $Ni_3(HITP)_2$ (Fig. 2a and b), the morphology of $Co(OH)_2$@$Ni_3(HITP)_2$ (Fig. 2d and e) looks much denser than that of $Ni_3(HITP)_2$. Moreover, the aligned pores are visible in the cryo-TEM image of $Ni_3(HITP)_2$, but similar structures cannot be detected in $Co(OH)_2$@$Ni_3(HITP)_2$ with the same imaging parameters. This is also shown by the line intensity profiles of the selected areas in the images, which show periodical intensity change for $Ni_3(HITP)_2$ corresponding to the $Ni_3(HITP)_2$ pores (Fig. 2c). The pore size of $Ni_3(HITP)_2$ is mostly measured to be ~2–4 nm as a result of the misaligned stacking among the $Ni_3(HITP)_2$ layers, which is slightly higher than the BET results (ESI Fig. 8c and d†). For $Co(OH)_2$@$Ni_3(HITP)_2$, the intensity changes are smaller and less ordered, indicating that the pores are filled with $Co(OH)_2$ NPs (Fig. 2f). The $Co(OH)_2$ NPs are measured to be ~1.2 ± 0.26 nm (Fig. 2e), which also matches with the pore size of $Ni_3(HITP)_2$ (~1.6 nm) on CNTs (ESI Fig. 8d†). Overall, the $Co(OH)_2$ NPs are confirmed to be confined in the pores of Ni_3(-HITP)$_2$ with the assistance of FESEM, TEM, BET and cryo-TEM characterizations, which can also be expected in the case of $Ni(OH)_2$@$Ni_3(HITP)_2$.

2.2 Hydrogen bonding (O···H–N) network between $Ni(OH)_2$ and $Ni_3(HITP)_2$

To understand the chemical interaction between TMH NPs and $Ni_3(HITP)_2$ in the hierarchical structure of TMH

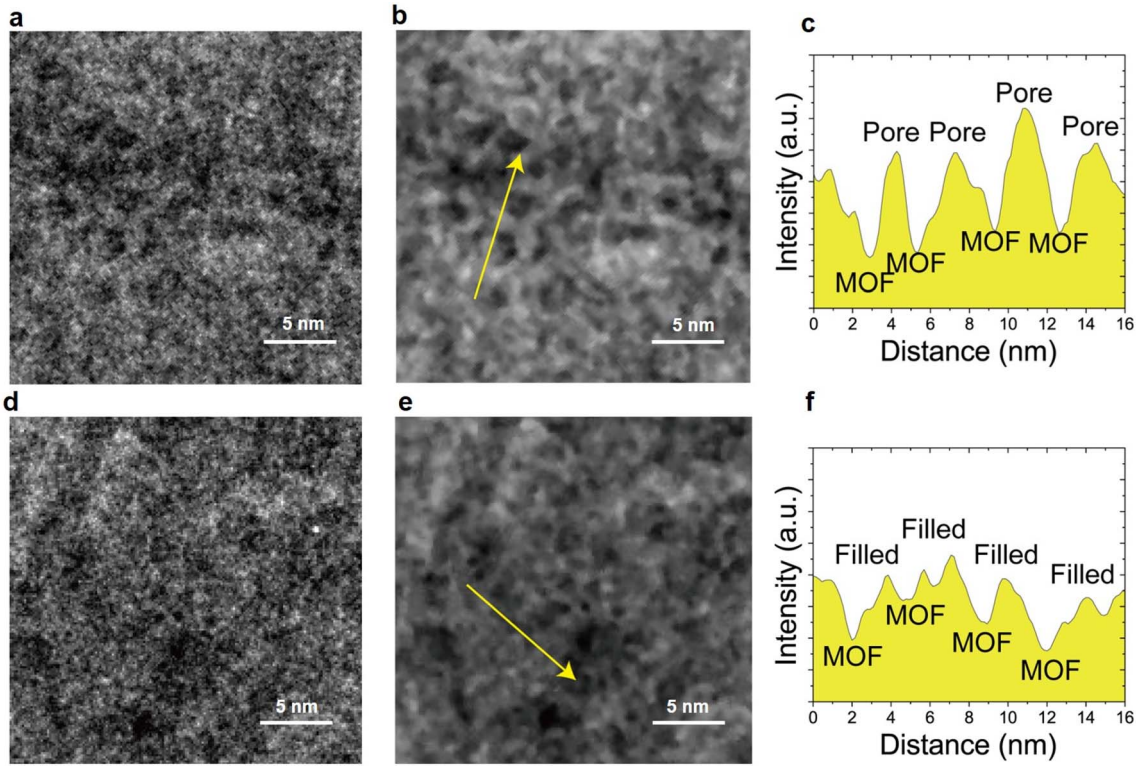

Fig. 2 Cryo-TEM images before and after median filtering (radius 2 pixels) and intensity profiles (yellow arrow highlighted areas) of (a–c) $Ni_3(HITP)_2$ and (d–f) $Co(OH)_2$@$Ni_3(HITP)_2$.

NPs@$Ni_3(HITP)_2$ on CNTs, we further performed experimental characterizations (X-ray diffraction (XRD), Raman, Fourier transform infrared spectroscopy (FTIR), and X-ray photoelectron spectroscopy (XPS)) and density functional theory (DFT) calculations. In the XRD patterns (Fig. 3a), the prominent peaks of $Ni_3(HITP)_2$ at $2\theta = 4.7°$, 9.5°, 12.6°, 16.5° and 27.4° confirm its crystalline structure.[28] However, only the peak at $2\theta = 4.7°$ in $Ni_3(HITP)_2$ (Inset of Fig. 3a) is detected for $Ni_3(HITP)_2$@CNT, $Ni(OH)_2$@$Ni_3(HITP)_2$@CNT and $Co(OH)_2$@$Ni_3(HITP)_2$@CNT, which is probably due to the overwhelmed signals from CNTs that completely mask those of $Ni_3(HITP)_2$.[29,30] Furthermore, the weak peak of β-$Ni(OH)_2$ at $2\theta = 38.4°$ and the peaks of β-$Co(OH)_2$ at $2\theta = 38.0°$ and 39.0° prove (ESI Fig. 9†) the incorporation of $Ni(OH)_2$ and $Co(OH)_2$ in $Ni_3(HITP)_2$@CNT, respectively.[31,32] Additionally, 2D $Ni_3(HITP)_2$ possesses a similar extended conjugated π-structure to CNTs with respect to both geometric and electronic structures, which benefits its growth on CNTs.[33] In Raman spectra, we found that the peak intensity of G band in $Ni_3(HITP)_2$@CNT is higher than that in CNTs. The intensity ratio of D and G bands calculated from the band area in $Ni(OH)_2$@$Ni_3(HITP)_2$@CNT (~0.04) and $Co(OH)_2$@$Ni_3(HITP)_2$@CNT (~0.02) is slightly lower than that in CNTs (~0.05), indicating enhanced π–π conjugation interaction between the $Ni_3(HITP)_2$ ligand and CNTs (ESI Fig. 10†).[34,35]

In FTIR spectra (Fig. 3b), the observed peaks at 1640, 1557 and 1385 cm^{-1} are assigned to –N–H (or –C–C), –C=C and –C–C vibrations in CNTs and $Ni_3(HITP)_2$. The peak at 1259 cm^{-1} corresponds to the –C–N bond in the HITP ligand. And the wide peaks at 540 and 520 cm^{-1} are assigned to the –Ni–O bond and –Co–O bond, respectively.[36,37] Interestingly, the band at ~803 cm^{-1} in $Ni_3(HITP)_2$ and $Ni_3(HITP)_2$@CNT can be assigned to the out-of-plane bending vibration of the –NH group from the HITP ligands, and this band shows a small red shift to ~798 cm^{-1} in $Ni(OH)_2$@$Ni_3(HITP)_2$@CNT and to ~800 cm^{-1} in $Co(OH)_2$@$Ni_3(HITP)_2$@CNT, respectively (Inset of Fig. 3b). It is probably caused by the formation of hydrogen bonding (H-bonding) (X–H···Y, where X is proton donor and Y is proton acceptor). As the H-bonding interaction is predominantly electrostatic, the electronegative element Y attracts the hydrogen toward itself, which can lengthen the X–H bond and the corresponding red-shift of the X–H vibration frequency.[38,39] In addition, it is also possible to estimate thermodynamic properties related to H-bonding from the FTIR data using the empirical correlations between the H-bonding energy and the red-shift of ν_4 mode band corresponding to the bending vibration ($-\Delta H^2 = 0.67\Delta{\nu_4}^2$, and $\Delta{\nu_4}^2 = 10^{-4}[(\nu_4^{H})^2 - (\nu_4^{0})^2]$, where ν_4^{H} (cm^{-1}) is the H-bonded X–H bond, ν_4^{0} (cm^{-1}) is the free X–H bond, and ΔH (kJ mol^{-1}) is the H-bonding energy).[40] H-bonding energy was calculated to be 0.54 kJ mol^{-1} in $Ni(OH)_2$@$Ni_3(HITP)_2$@CNT and 0.32 kJ mol^{-1} in $Co(OH)_2$@$Ni_3(HITP)_2$@CNT, respectively, which indicates that $Ni(OH)_2$@$Ni_3(HITP)_2$@CNT and $Co(OH)_2$@$Ni_3(HITP)_2$@CNT are more stable than $Ni_3(HITP)_2$@CNT due to the energy release. Moreover, the peaks at 855.6 eV and 857.2 eV in XPS spectra (Fig. 3c) originate from

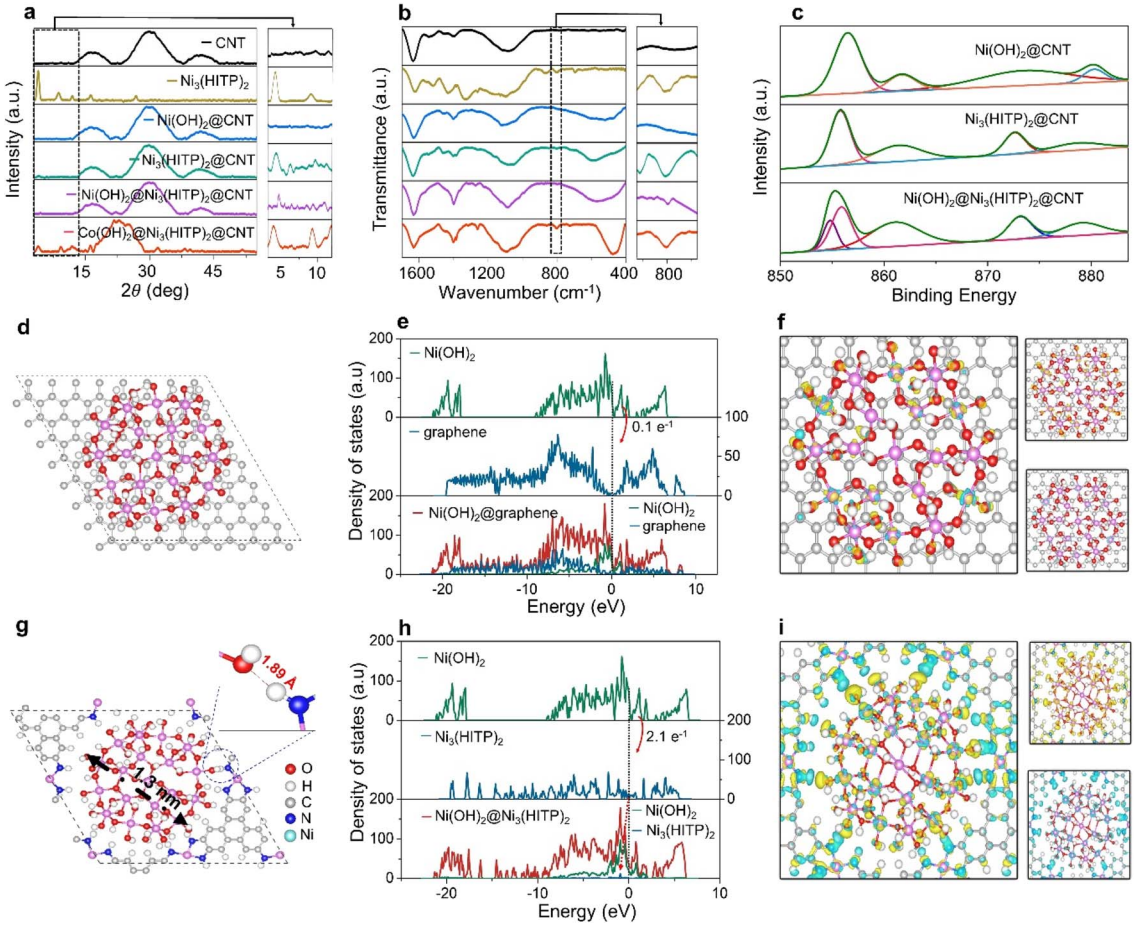

Fig. 3 (a) XRD patterns and (b) FTIR spectra of the prepared CNT film-based samples. (c) XPS peaks of Ni 2p in the prepared CNT film-based samples. Schematic illustration of the geometric structure, DFT-calculated partial density of states (PDOS) and differential charge density isosurfaces of (d–f) $Ni(OH)_2$@graphene and (g–i) $Ni(OH)_2$ in $Ni_3(HITP)_2$, respectively. The yellow and blue colors denote the charge accumulation and charge depletion, respectively. Note: (1) CNT films instead of CNTYs were used to synthesize five types of large samples for XRD and FTIR characterizations, where the raw CNT materials in CNTYs and CNT films are the same. (2) Insets of (a) and (b) show the XRD patterns from $2\theta = 3°$ to $2\theta = 12°$, and FTIR spectra from 750 cm^{-1} to 850 cm^{-1}, respectively. (3) To simplify the DFT models, a single-layered graphene was used to substitute CNTs during simulation process. The cluster size of $Ni(OH)_2$ is 1.3 nm in the DFT calculations.

Ni^{2+} and Ni^{3+}, respectively.[30,41,42] It suggests the formation of hyper-hydroxylation of $Ni(OH)_2$ NPs, which probably corresponds to the formation of H-bonding between $Ni_3(HITP)_2$ and $Ni(OH)_2$ NPs.[43] In this work, the possible H-bonding can be the O–H···N bond formed between –NH from $Ni_3(HITP)_2$ and O from $Ni(OH)_2$ or the N···H–O bond between N from $Ni_3(HITP)_2$ and –OH from $Ni(OH)_2$. To our knowledge, the electronegativity of O is higher than that of N, thus we believe that the formed H-bonding is likely to be the O–H···N bond.

DFT calculations were performed to give further insights into the formation of H-bonding between $Ni_3(HITP)_2$ and $Ni(OH)_2$ NPs (ESI Scheme 1†). The DFT results show that the adsorption energy for $Ni(OH)_2$ cluster absorbed on graphene and $Ni_3(HITP)_2$ is −0.41 eV and −2.90 eV, respectively. Structural analysis reveals that the strong adsorption of $Ni(OH)_2$ cluster on $Ni_3(HITP)_2$ originates from the 12 H-bonds (O···H–N) between –NH from $Ni_3(HITP)_2$ and –OH from the $Ni(OH)_2$ cluster (Fig. 3d and g). Bader charge analysis shows that the $Ni(OH)_2$ cluster transfers only −0.1 e^- to graphene while −2.1 e^- to $Ni_3(HITP)_2$ (Fig. 3e and h), which is in accordance with the calculated adsorption energy results. The more negative adsorption energy and more charge transfer mean the stronger binding ability between $Ni(OH)_2$ and $Ni_3(HITP)_2$. And the partial density of states (PDOS) of $Ni(OH)_2$ cluster changes little before and after $Ni(OH)_2$ adsorption on graphene while the Fermi energy moves down ∼−3 eV when $Ni(OH)_2$ cluster adsorbs on $Ni_3(HITP)_2$ (Fig. 3h). In contrast, the Fermi energy of graphene remains unchanged while the Fermi energy of $Ni_3(HITP)_2$ moves up ∼2 eV after the $Ni(OH)_2$ cluster adsorbs on it (Fig. 3e). The more negative value of the Fermi energy of $Ni(OH)_2$ cluster indicates a much higher stability of $Ni(OH)_2$ adsorbing on $Ni_3(HITP)_2$. The differential charge density ($\Delta\rho$) ($\Delta\rho = \rho$(heterojunction) − ρ($Ni(OH)_2$) − ρ(substrate)) of the two heterojunctions is plotted to explore the bonding behavior between the $Ni(OH)_2$ cluster and the supporting substrate. We find that there is little charge transfer between $Ni(OH)_2$ cluster and

graphene (Fig. 3f), while there is an obvious charge accumulation for O atoms around the edge of the cluster and a charge deletion for H atoms of –NH (Fig. 3i) from $Ni_3(HITP)_2$, which indicates the strong interaction between $Ni(OH)_2$ cluster and $Ni_3(HITP)_2$ is dominated by the p_z orbital of O atoms from –OH and the s orbital of H from –NH. This result means that O atoms of –OH and H atoms of –NH form H-bonding. Additionally, the calculated length of the –N–H bond in $Ni_3(HITP)_2$ is 1.019 Å, which is slightly shorter than that in $Ni(OH)_2@Ni_3(HITP)_2$ cluster (1.053 Å). It aligns well with the red shift in FTIR spectra (Fig. 3b). Similar to that in $Ni(OH)_2@Ni_3(HITP)_2$, when $Ni_3(HITP)_2$ is filled with $Co(OH)_2$ NPs , the –N–H bond also becomes longer because the formed H-bonding is assigned to O–H···N, which indicates that these results from DFT calculations are also applicable to $Co(OH)_2@Ni_3(HITP)_2$. Overall, the type of H-bonding formed between $Ni_3(HITP)_2$ and TMH NPs ($Ni(OH)_2$ and $Co(OH)_2$ NPs) is the O–H···N bond.

2.3 Electrochemical performance and applications

In order to assess the effectiveness of the ship-in-a-bottle hierarchical structure of $Ni(OH)_2@Ni_3(HITP)_2$, the electrochemical performance of CNTY-based electrodes has been evaluated by cyclic voltammetry (CV), galvanostatic charge/discharge (GCD) and electrochemical impedance spectra (EIS), respectively. The binary $Ni_3(HITP)_2@CNTY$ electrodes with different synthesis time were first characterized in sulfuric acid/polyvinyl alcohol (H_2SO_4/PVA) to ensure an optional synthesis parameter. As shown in ESI Fig. 11–12,† compared to CNTY electrode, $Ni_3(HITP)_2@CNTY_{(2)}$ electrode and $Ni_3(HITP)_2@CNTY_{(4)}$ electrode, $Ni_3(HITP)_2@CNTY$ electrode exhibits the biggest closed area in CV measurements and the longest discharge time in GCD curves. Additionally, $Ni_3(HITP)_2@CNTY$ electrode reaches up to 340 mF cm^{-2} at 0.1 mA cm^{-2} due to the abundant ion accessible active sites provided by $Ni_3(HITP)_2$, further indicating that proper loading of $Ni_3(HITP)_2$ can tune the electrochemical performance of CNTYs.

The ternary TMH NPs@$Ni_3(HITP)_2@CNTY$ electrodes in potassium hydroxide/polyvinyl alcohol (KOH/PVA) gel electrolyte were investigated to gain insights into the effect of ship-in-a-bottle architecture on the electrochemical performance, especially the cyclic performance. Additionally, we chose KOH/PVA stead of H_2SO_4/PVA to characterize the electrochemical performance of the ternary TMH NPs@$Ni_3(HITP)_2@CNTY$ electrodes to fully release the pseudocapacitive performance of TMH NPs, since H_2SO_4/PVA causes the corrosion of TMH NPs. $Ni(OH)_2@Ni_3(HITP)_2@CNTY$ SC and $Co(OH)_2@Ni_3(HITP)_2@CNTY$ SC show strong redox features due to the redox reactions $(Ni(II)_3(HITP)_2 \rightleftarrows Ni(III)_3(HITP)_2 + e^-$, $Ni(OH)_2 + OH^- \rightleftarrows NiOOH + H_2O + e^-$, $Co(OH)_2 + OH^- \rightleftarrows CoOOH + H_2O + e^-$ and $CoOOH + OH^- \rightleftarrows CoO_2 + H_2O + e^-)$ (Fig. 4a and ESI Fig. 13a, c, e and g†), while the $Ni_3(HITP)_2@CNTY$ SC displays an approximately rectangle-like CV curve.[44]

In order to better understand the kinetics and charge storage mechanism of the binary and ternary electrodes, the CV data were analyzed with Dunn's method by calculating the b value from the equation $i(v) = av^b$ at different scan rates to clarify the capacitive contribution and the diffusion-controlled

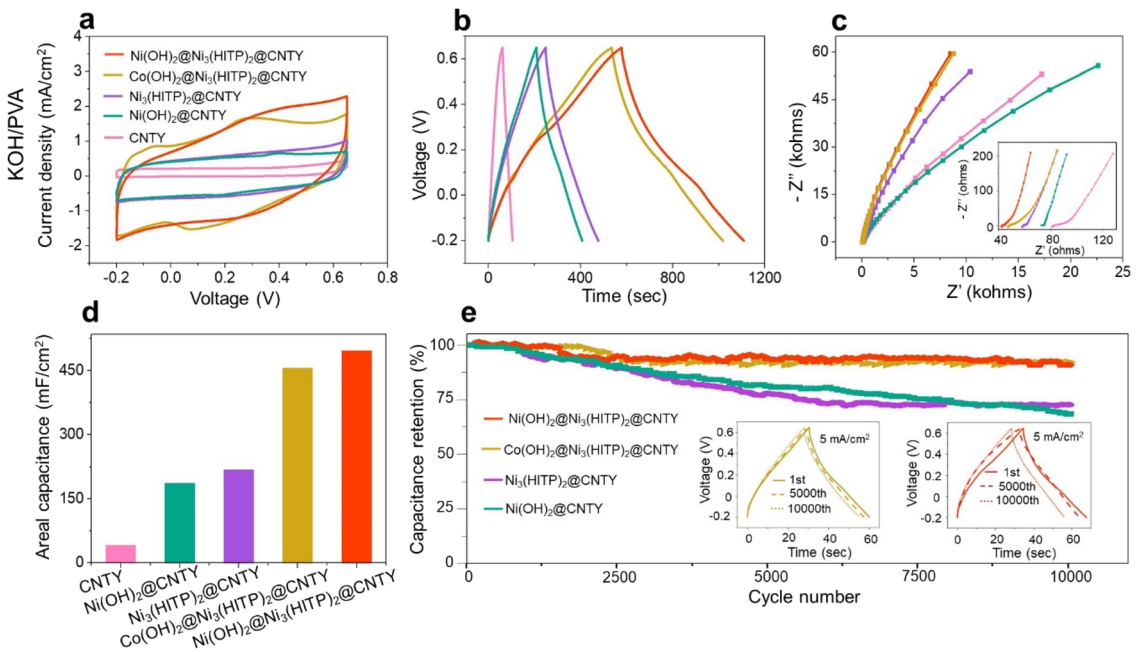

Fig. 4 Electrochemical performance of CNTY-based SCs in a two-electrode system. (a–c) CV curves at 5 mV s^{-1}, GCD curves at 0.4 mA cm^{-2} and the EIS test of CNTY-based SCs in 2 M KOH/PVA gel electrolyte, respectively. (d) A summary of calculated C_A values from (b). (e) The cyclic life of the quasi-solid-state $Ni(OH)_2@Ni_3(HITP)_2@CNTY$ SC and $Co(OH)_2@Ni_3(HITP)_2@CNTY$ SC, $Ni_3(HITP)_2@CNTY$ SC and $Ni(OH)_2@CNTY$ SC at 5 mA cm^{-2} in 2 M KOH/PVA gel electrolyte. Note: Insets of (e) show selected GCD curves (1st, 5000th, and 10 000th) of $Ni(OH)_2@Ni_3(HITP)_2@CNTY$ SC and $Co(OH)_2@Ni_3(HITP)_2@CNTY$ SC.

contribution, where i is the measured current at a given potential, a and b are parameters calculated from the equation and v is the scan rate. The capacitive-type storage gives $b = 1$, while the diffusion-limited process gives $b = 0.5$.[45,46] Herein, $Ni(OH)_2$@$Ni_3(HITP)_2$@CNTY electrode and $Co(OH)_2$@$Ni_3(HITP)_2$@CNTY electrode exhibit both capacitive behavior and diffusion-controlled behavior, since the b value of $Ni(OH)_2$@$Ni_3(HITP)_2$@CNTY electrode and $Co(OH)_2$@$Ni_3(HITP)_2$@CNTY electrode is 0.73 and 0.79, respectively (ESI Fig. 14a, c, e and g†). Furthermore, the quantitative examination of the contribution from the surface capacitive effect and diffusion-controlled insertion is carried out by expressing the current response as the combination of these two processes $i(v) = k_1v + k_2v^{1/2}$, where k_1v and $k_2v^{1/2}$ correspond to the current contributions from the surface capacitive effects and the diffusion-controlled intercalation process, respectively.[47] The intercalation capacitive contribution of $Ni(OH)_2$@$Ni_3(HITP)_2$@CNTY SC increases from 31.4% at 5 mV s^{-1} to 75.6% at 200 mV s^{-1}, while that of $Co(OH)_2$@$Ni_3(HITP)_2$@CNTY SC increases from 44.1% to 84.6% at the same scan rate (ESI Fig. 14b, d, f and h†). The gradually enhanced capacitive behavior enables fast charging and discharging, thus demonstrating high power characteristics.[48]

The nearly symmetric GCD curves of the ternary CNTY-based SCs display pseudocapacitance behavior (Fig. 4b and ESI Fig. S13b, d, f and h†), demonstrating their excellent electrochemical reversibility and good coulombic efficiency. Additionally, $Ni(OH)_2$@$Ni_3(HITP)_2$@CNTY SC displays the longest discharge time (~527.0 s) at 0.4 mA cm^{-2} among the prepared SCs. The C_A calculated from the GCD curve of the $Ni(OH)_2$@$Ni_3(HITP)_2$@CNTY electrode (496.0 mF cm^{-2} or 331.8 F g^{-1} or 208.9 F cm^{-3} at 0.4 mA cm^{-2}) is ~2.1-fold that of the $Ni_3(HITP)_2$@CNTY electrode (217.6 mF cm^{-2} or 155.2 F g^{-1} or 93.8 F cm^{-3} at 0.4 mA cm^{-2}) and ~2.7-fold that of $Ni(OH)_2$@CNTY electrode (186.4 mF cm^{-2} or 120.6 F g^{-1} or 81.4 F cm^{-3} at 0.4 mA cm^{-2}) (Fig. 4d and ESI Fig. 15a†). The $Ni(OH)_2$@$Ni_3(HITP)_2$@CNTY electrode shows an energy density of 49.8 μW h cm^{-2} at a power density of 340.0 μW cm^{-2} (or 33.3 mW h g^{-1} at 227.5 mW g^{-1} or 30.0 mW h cm^{-3} at 143.2 mW cm^{-3}) (ESI Fig. 15b†). Compared to reported $Ni(OH)_2$-based symmetric SCs, the energy density and power density in our work outperform the majority of them (ESI Table 2†).

In addition, the Coulomb efficiency of $Ni(OH)_2$@$Ni_3(HITP)_2$@CNTY and $Co(OH)_2$@$Ni_3(HITP)_2$@CNTY electrodes at 0.4 mA cm^{-2} is 85.8% and 88.1%, respectively. All electrodes show unobvious *IR* drops. Moreover, the *IR* drop of $Ni(OH)_2$@$Ni_3(HITP)_2$@CNTY SC (Fig. 4b) (~5.4 mV) is lower than that of $Ni_3(HITP)_2$@CNTY SC (~14.1 mV) and $Ni(OH)_2$@CNTY SC (~9.1 mV), indicating ultralow charge-transfer resistance and low internal resistance, which is further confirmed by EIS tests.[49] The conducting $Ni_3(HITP)_2$ network with nanoconfined $Ni(OH)_2$ NPs facilitates both ion and electron transport between electrochemical materials and electrolyte.[50] The ESR values of $Ni(OH)_2$@$Ni_3(HITP)_2$@CNTY SC (~42.5 Ω) and $Co(OH)_2$@$Ni_3(HITP)_2$@CNTY SC (~47.5 Ω) are much lower than that of $Ni_3(HITP)_2$@CNTY SC (~58.2 Ω) and $Ni(OH)_2$@CNTY SC (~72.9 Ω), and CNTY SC (~80.8 Ω), indicating the lower interface resistance between active materials and the current collector in TMH NPs@$Ni_3(HITP)_2$@CNTY SCs (Inset of Fig. 4c).[6] Additionally, the large ESR value in CNTY-based SC is a common problem, which can be attributed to the small cross-sectional area of CNTY that gives rise to the increased resistance to electrical current flowing along CNTY-based electrodes during charging/discharging processes.[51] Meanwhile, it should be noted that for TMH NPs@$Ni_3(HITP)_2$@CNTY SCs, smaller semicircles are observed compared to those of $Ni(OH)_2$@CNTY and CNTY, demonstrating a lower interfacial charge-transfer resistance (R_{ct}).[52] The slope of the $Ni(OH)_2$@$Ni_3(HITP)_2$@CNTY SC shows the highest gradient of Warburg in its Nyquist plot, indicating its low resistance to the electrolyte ions diffusing to the electrode surface (R_d) (Fig. 4c). For more specific analysis, we fitted the EIS data of TMH NPs@$Ni_3(HITP)_2$@CNTY SCs using the Z-view software. The fitting results are in great accordance with the raw data (ESI Fig. 16†). The corresponding fitted ESR values are 42.9 Ω for the $Ni(OH)_2$@$Ni_3(HITP)_2$@CNTY SC and 48.3 Ω for $Co(OH)_2$@$Ni_3(HITP)_2$@CNTY SC, which confirm the suitability of the used equivalent circuit model and support the above discussion well (ESI Table 3†).

More importantly, the capacitance retentions of $Ni(OH)_2$@$Ni_3(HITP)_2$@CNTY SC and $Co(OH)_2$@$Ni_3(HITP)_2$@CNTY SC (Fig. 4e) only show a slight reduction to 90.9% and 92.3% after 10 000 cycles at 5 mA cm^{-2}, respectively, which outperforms that of $Ni_3(HITP)_2$@CNTY SC (72.6%) and $Ni(OH)_2$@CNTY SC (68.4%). Besides, 90% performance of the ternary electrodes was maintained when the SC is bent at different angles and after bending 3000 cycles, indicating an excellent flexibility of the SCs (ESI Fig. 17†). The excellent cyclic life is ascribed to the synergistic effect in their hierarchical structure because $Ni_3(HITP)_2$ can sturdily grow on CNTs by π–π interaction and the H-bonding network between the conducting nanoporous network and nanoconfined TMH NPs can mutually lock each other.

To further explore the relationship between the special structure and cyclic life, we characterized the morphology of the electrodes after 10 000 cycles in a two-electrode system (Fig. 5a–d). For $Ni(OH)_2$@CNTY electrode, the surface of CNTs after cycling is almost as smooth as that of pristine CNTs (ESI Fig. 2a†), suggesting the peeling-off of the majority of $Ni(OH)_2$ NPs from CNT surface (Fig. 1b and 5a). For $Ni_3(HITP)_2$@CNTY electrode, $Ni_3(HITP)_2$ after cycling was partially exfoliated from the CNT surface (Fig. 1d and 5b), owing to the structural collapse of $Ni_3(HITP)_2$ caused by the repeated volumetric change of $Ni_3(HITP)_2$ and decomposition of metal coordination from chemical weak points at the metal (Ni^{2+} ions) nodes. However, TMH NP@$Ni_3(HITP)_2$ on the ternary electrode (Fig. 5c and d) still remains intact after cycling, echoing its high capacitance retention. These hybrid electrodes were further characterized by XRD and FTIR after 10 000 charging/discharging cycles in a two-electrode system. The peak at $2\theta = 4.7°$ in $Ni_3(HITP)_2$@CNT, $Ni(OH)_2$@$Ni_3(HITP)_2$@CNT and $Co(OH)_2$@$Ni_3(HITP)_2$@CNT electrodes still appears after cycling (Fig. 5e). In comparison to its original XRD pattern (Fig. 3a), the peak at $2\theta = 9.5°$ weakens and shifts towards the lower angle in $Ni_3(HITP)_2$@CNT, indicating the deteriorated crystal structure of $Ni_3(HITP)_2$@CNT electrode after cycling

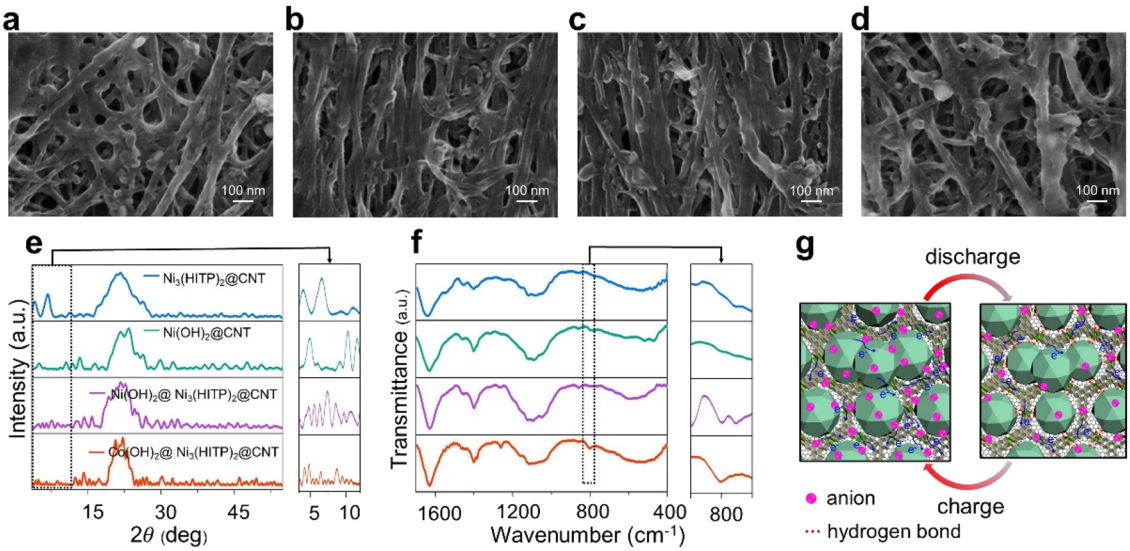

Fig. 5 (a–d) FESEM images of $Ni(OH)_2$@CNT, $Ni_3(HITP)_2$@CNT, $Ni(OH)_2$@$Ni_3(HITP)_2$@CNT and $Co(OH)_2$@$Ni_3(HITP)_2$@CNT electrodes after 10 000 cycles. (e and f) XRD patterns and FTIR spectra of four types of samples after 10 000 cycles in a two-electrode system. Note: The CNTs in CNTYs and CNT films have no differences. (g) A proposed charge storage and transfer mechanism in the positive TMH NPs @$Ni_3(HITP)_2$@CNT electrode.

(Inset of Fig. 5e). Additionally, the peak at $2\theta = 38.4°$ in the $Ni(OH)_2$@$Ni_3(HITP)_2$@CNT electrode still remains after cycling, but the peaks at $2\theta = 38°$ and 39° in the $Co(OH)_2$@$Ni_3(HITP)_2$@CNT electrode disappear or shift to higher angles (ESI Fig. 18†), indicating a stable structure of $Ni(OH)_2$@$Ni_3(HITP)_2$@CNT electrode. In FTIR spectra (Fig. 5f), $Ni(OH)_2$@CNT electrode obtains the highest degree of phase transition since the wide peak at ~540 cm^{-1} exhibits obvious deformation after cycling, and the weak peaks at ~798 and ~777 cm^{-1} are generated due to the interaction between KOH/PVA gel electrolyte and the $Ni(OH)_2$@CNT electrode after cycling. In $Ni_3(HITP)_2$@CNT electrode, the transmittance intensity of the peak at 1259 cm^{-1} is weakened and the peak at ~803 cm^{-1} for the –NH group is significantly diminished after cycling, indicating the partial exfoliation of $Ni_3(HITP)_2$ on CNTs. However, those in TMH NPs@$Ni_3(HITP)_2$@CNT electrodes are almost constant. Moreover, the peaks for H-bonding at ~798 cm^{-1} in $Ni(OH)_2$@$Ni_3(HITP)_2$@CNT electrode and ~800 cm^{-1} in $Co(OH)_2$@$Ni_3(HITP)_2$@CNT electrode remain. These results further confirm that H-bonding between TMH NPs and $Ni_3(HITP)_2$ improves the structural stability of the ternary electrodes. Therefore, we conjecture that this ship-in-a-bottle architecture can support the whole framework of TMH NPs@$Ni_3(HITP)_2$ and buffer the attack from electrolyte during cycling toward significantly enhanced structural stability and electrochemical performance.

Fig. 5g demonstrates the charge storage and transfer mechanism in the positive ternary-based electrodes. The hierarchical TMH NPs@$Ni_3(HITP)_2$ enables the access of electrolyte and provides shortened diffusion path lengths as well, which is beneficial for rapid adsorption/disadsorption of ions and electrons. The nanoconfined TMH NPs in microporous $Ni_3(HITP)_2$ hold limited swelling/shrinking and H-bonding between $Ni_3(HITP)_2$ and TMH NPs supports the framework of $Ni_3(HITP)_2$ during charging/discharging process, collectively leading to a stable system for ultrahigh cyclic life. Therefore, the ship-in-a-bottle nanostructure can provide synergistic impact on the ternary-based electrodes toward high efficiency in electrolyte ion storage, charge transfer and ultrastable cyclic performance.

Finally, we compared the electrochemical properties of ternary-based SCs with those previously reported in references, including C_A (Fig. 6a),[53–65] energy density and power density (Fig. 6b)[53–57,59–64] and cyclic performance (Fig. 6c).[53–58,60–63] In detail, $Ni(OH)_2$@$Ni_3(HITP)_2$@CNTY electrode exhibits excellent charge storage capability with a high energy density of 49.8 μW h cm^{-2} at 340.0 μW cm^{-2} (calculated based on yarn electrode), which is higher than that of MOF modified yarn-based SCs,[53,54] pseudocapacitive material modified carbon yarn-based SCs[55–61] and most of functionalized commercial yarn-based SCs[62–65] (Fig. 6a and b). Besides, the stability of TMH NPs@$Ni_3(HITP)_2$@CNTY SCs demonstrates superior cycle life (Fig. 6c). Moreover, the tensile property of $Ni(OH)_2$@$Ni_3(HITP)_2$@CNTY (~13 MPa) (ESI Fig. 19†) remain similar to that of pristine CNTY, suggesting good mechanical property and knit ability. Finally, we demonstrated the potential applications using our optimized CNTY-based SCs for powering up wearable electronics. Additionally, the assembled SCs in series connection exhibit approximately a proportional working voltage window in GCD curves at 5 mA cm^{-2}, indicating the near uniformity of the assembled SC (ESI Fig. 20†). The sweater integrated with in-series SCs can provide enough electricity to power up electronic devices, such as an electronic watch (KK-907, 1.5 V/5 μW), a pedometer (Meilen, mj001, 1.5 V/75 μW), a thermo-hygrometer (MITIR, 1.5 V/30 μW), and an ultraviolet detector (MEET, MS-98(3), 3 V/30 μW) (Fig. 5d–g and ESI Fig. 21†).

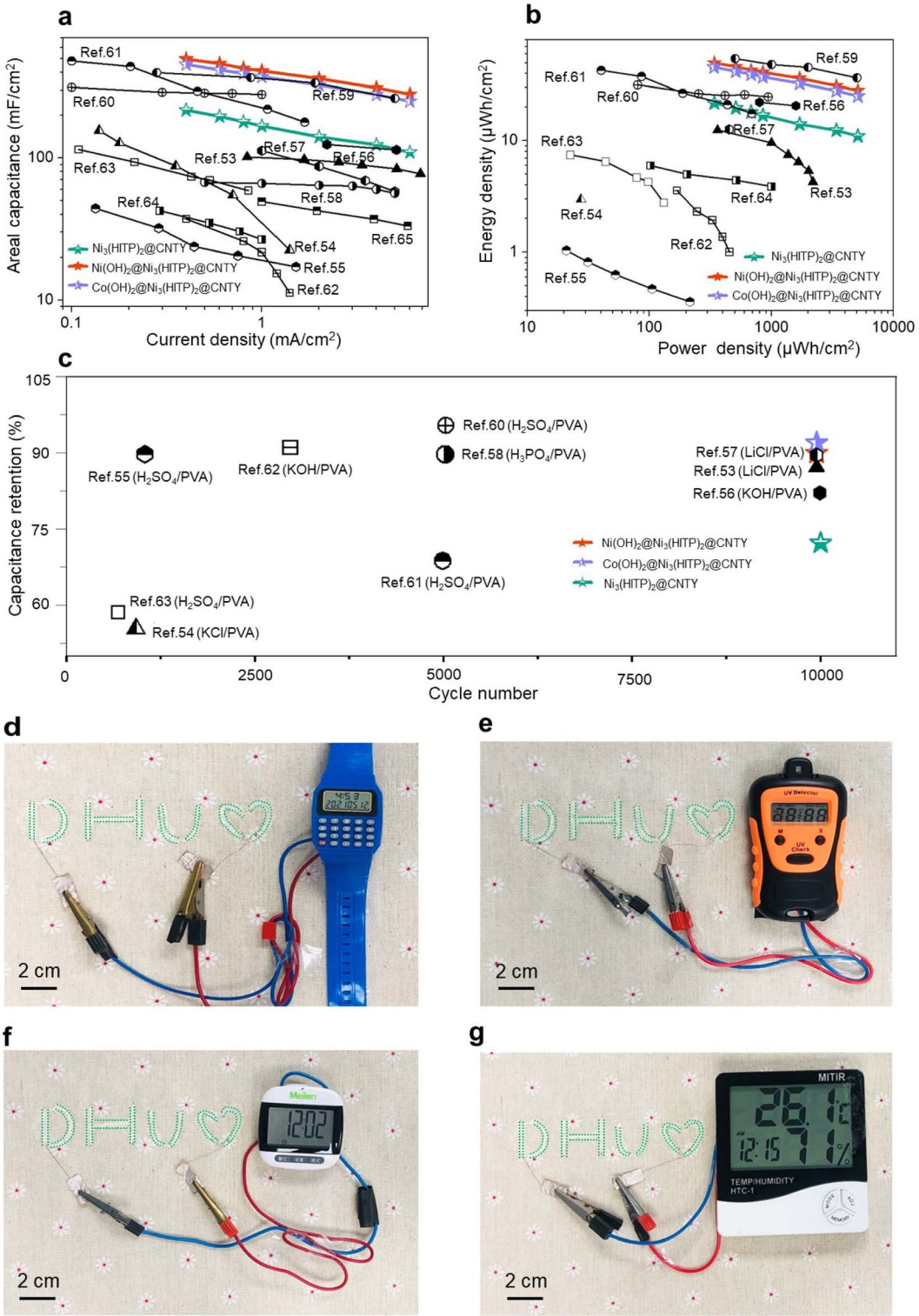

Fig. 6 Performance comparison and application. (a) C_A, (b) Ragone plots of energy density and power density, and (c) cyclic performance of our ternary-based SCs and other reported fiber or yarn shaped SCs in literature. (d–g) Digital photo images of various electronics powered by our ternary-based SCs, which are marked using green dotted lines.

3. Conclusion

In summary, we developed a facile route to fabricate CNTY-based SCs with a unique ship-in-a-bottle architecture by *in situ* growing conducting $Ni_3(HITP)_2$ filled with TMH NPs ($Ni(OH)_2$ and $Co(OH)_2$). The nanoconfinement is confirmed by FESEM, TEM, EDS, BET and cryo-TEM characterization studies. On the other hand, the H-bonding (O···H–N) network between

TMH NPs and $Ni_3(HITP)_2$ is verified by FTIR and DFT calculations. Both nanoconfinement and the H-bonding network are confirmed to contribute to the ultra-stable electrochemical performance in the ternary TMH NPs@$Ni_3(HITP)_2$@CNTY structures.

Data availability

The data supporting our findings in this work are available from the corresponding author K. Z. upon reasonable request.

Author contributions

Prof. K. Z. conceived the idea and designed the experiments. Prof. K. Z. and Prof. B. W. supervised the project. Q. X. carried out the sample synthesis, characterization studies, and electrochemical measurements. Dr X. L. conducted DFT calculations and related analysis. M. Z. and Prof. B. X. performed the synthesis of HATP·6HCl. Prof. Y. X contributed to the cryo-TEM imaging. All authors contributed to the writing, review and editing of the manuscript.

Conflicts of interest

The authors declare no conflict of interest.

Acknowledgements

Prof. K. Zhang is grateful to the funding support from the Fundamental Research Fund for the Central Universities (2232022G-01 and 19D110106), the National Natural Science Foundation of China (no. 51973034), the Young Elite Scientists Sponsorship Program by CAST (2017QNRC001) and Graduate Student Innovation Fund of Donghua University (20D310111).

References

1 L. Kou, T. Huang, B. Zheng, Y. Han, X. Zhao, K. Gopalsamy, H. Sun and C. Gao, *Nat. Commun.*, 2014, **5**, 3754–3764.
2 C. Yang, Q. Liu, L. Zang, J. Qiu, X. Wang, C. Wei, X. Qiao, L. Hu, J. Yang, G. Song and C. Liu, *Adv. Electron. Mater.*, 2019, **5**, 1800435–1800444.
3 J. Ren, L. Li, C. Chen, X. Chen, Z. Cai, L. Qiu, Y. Wang, X. Zhu and H. Peng, *Adv. Mater.*, 2013, **25**, 1155–1159.
4 S. Pan, H. Lin, J. Deng, P. Chen, X. Chen, Z. Yang and H. Peng, *Adv. Electron. Mater.*, 2015, **5**, 1401438–1401445.
5 D. Zhang, M. Miao, H. Niu and Z. Wei, *ACS Nano*, 2014, **8**, 4571–4579.
6 Z. Lu, Y. Chao, Y. Ge, J. Foroughi, Y. Zhao, C. Wang, H. Long and G. G. Wallace, *Nanoscale*, 2017, **9**, 5063–5071.
7 Z. Lu, R. Raad, F. Safaei, J. Xi, Z. Liu and J. Foroughi, *Front. Mater.*, 2019, **113**, 151–158.
8 Z. Lu, J. Foroughi, C. Wang, H. Long and G. G. Wallace, *Adv. Energy Mater.*, 2017, **8**, 1702047–1702057.
9 C. Choi, H. J. Sim, G. M. Spinks, X. Lepró, R. H. Baughman and S. J. Kim, *Adv. Energy Mater.*, 2016, **6**, 1502119–1502142.
10 C. Lu, J. Meng, J. Zhang, X. Chen, M. Du, Y. Chen, C. Hou, J. Wang, A. Ju, X. Wang, Y. Qiu, S. Wang and K. Zhang, *ACS Appl. Mater. Interfaces*, 2019, **11**, 25205–25217.
11 Q. Wang, D. Zhang, Y. Wu, T. Li, A. Zhang and M. Miao, *Energy Technol.*, 2017, **5**, 1449–1456.
12 Y. Zhou, X. Wang, L. Acauan, E. Kalfon-Cohen, X. Ni, Y. Stein, K. K. Gleason and B. L. Wardle, *Adv. Mater.*, 2019, **31**, 1901916–1901934.
13 G. Wang, L. Zhang and J. Zhang, *Chem. Soc. Rev.*, 2012, **41**, 797–828.
14 M. Zhi, C. Xiang, J. Li, M. Li and N. Wu, *Nanoscale*, 2013, **5**, 72–88.
15 T. Wang, H. C. Chen, F. Yu, X. S. Zhao and H. Wang, *Energy Storage Mater.*, 2019, **16**, 545–573.
16 H.-p. Feng, L. Tang, G.-m. Zeng, J. Tang, Y.-c. Deng, M. Yan, Y.-n. Liu, Y.-y. Zhou, X.-y. Ren and S. Chen, *J. Mater. Chem. A*, 2018, **6**, 7310–7337.
17 Y. Li, Q. Li, S. Zhao, C. Chen, J. Zhou, K. Tao and L. Han, *ChemistrySelect*, 2018, **3**, 13596–13602.
18 W.-H. Li, K. Ding, H.-R. Tian, M.-S. Yao, B. Nath, W.-H. Deng, Y. Wang and G. Xu, *Adv. Funct. Mater.*, 2017, **27**, 1702067.
19 D. Sheberla, J. C. Bachman, J. S. Elias, C. J. Sun, Y. Shao-Horn and M. Dinca, *Nat. Mater.*, 2017, **16**, 220–224.
20 R. A. Dodson, A. G. Wong-Foy and A. J. Matzger, *Chem. Mater.*, 2018, **30**, 6559–6565.
21 G. Xu, P. Nie, H. Dou, B. Ding, L. Li and X. Zhang, *Mater. Today*, 2017, **20**, 191–209.
22 A. J. Howarth, Y. Liu, P. Li, Z. Li, T. C. Wang, J. T. Hupp and O. K. Farha, *Nat. Rev. Mater.*, 2016, **1**, 15018.
23 D. Y. Lee, S. J. Yoon, N. K. Shrestha, S.-H. Lee, H. Ahn and S.-H. Han, *Microporous Mesoporous Mater.*, 2012, **153**, 163–165.
24 D. Zhang, Y. Zhu, L. Liu, X. Ying, C.-E. Hsiung, R. Sougrat, K. Li and Y. Han, *Science*, 2018, **359**, 675–679.
25 R. F. Egerton, *Microsc. Res. Tech.*, 2012, **75**, 1550–1556.
26 W. Zhou, X. Cao, Z. Zeng, W. Shi, Y. Zhu, Q. Yan, H. Liu, J. Wang and H. Zhang, *Energy Environ. Sci.*, 2013, **6**, 2216–2221.
27 L. Chen, H. Zhang, L. Chen, X. Wei, J. Shi and M. He, *J. Mater. Chem. A*, 2017, **5**, 22568–22575.
28 D. Sheberla, L. Sun, M. A. Blood-Forsythe, S. Er, C. R. Wade, C. K. Brozek, A. Aspuru-Guzik and M. Dinca, *J. Am. Chem. Soc.*, 2014, **136**, 8859–8862.
29 Q. Mu, W. Zhu, X. Li, C. Zhang, Y. Su, Y. Lian, P. Qi, Z. Deng, D. Zhang, S. Wang, X. Zhu and Y. Peng, *Appl. Catal., B*, 2020, **262**, 118144–118153.
30 D. Cai, M. Lu, L. Li, J. Cao, D. Chen, H. Tu, J. Li and W. Han, *Small*, 2019, **15**, 1902605–1902616.
31 X. Wang, J. Liu, Y. Wang, C. Zhao and W. Zheng, *Mater. Res. Bull.*, 2014, **52**, 89–95.
32 F. Cao, G. X. Pan, P. S. Tang and H. F. Chen, *J. Power Sources*, 2012, **216**, 395–399.
33 J. Liu, X. Song, T. Zhang, S. Liu, H. Wen and L. Chen, *Angew. Chem., Int. Ed.*, 2021, **60**, 5612–5624.
34 H. Yang, Q. Zhang, C. Shan, F. Li, D. Han and L. Niu, *Langmuir*, 2010, **26**, 6708–6712.

35 S. Sarkar, S. Niyogi, E. Bekyarova and R. C. Haddon, *Chem. Sci.*, 2011, **2**, 1326–1333.
36 W. Zhu, C. Zhang, Q. Li, L. Xiong, R. Chen, X. Wan, Z. Wang, W. Chen, Z. Deng and Y. Peng, *Appl. Catal., B*, 2018, **238**, 339–345.
37 K. Wang, X. Zhang, X. Zhang, D. Chen and Q. Lin, *J. Power Sources*, 2016, **333**, 156–163.
38 H. Sun, S. Liu, W. Lin, K. Y. Zhang, W. Lv, X. Huang, F. Huo, H. Yang, G. Jenkins, Q. Zhao and W. Huang, *Nat. Commun.*, 2014, **5**, 3601–3610.
39 H. Wang, Q. Hao, X. Yang, L. Lu and X. Wang, *Electrochem. Commun.*, 2009, **11**, 1158–1161.
40 S. Jarmelo, I. Reva, P. R. Carey and R. Fausto, *Vib. Spectrosc.*, 2007, **43**, 395–404.
41 F. Gu, X. Cheng, S. Wang, X. Wang and P. S. Lee, *Small*, 2015, **11**, 2044–2050.
42 Z. Wu, X. L. Huang, Z. L. Wang, J. J. Xu, H. G. Wang and X. B. Zhang, *Sci. Rep.*, 2014, **4**, 3669–3677.
43 Z. Ma, P. Wang and Y. Pei, *Nanoscale*, 2016, **8**, 17044–17054.
44 T. Nguyen, M. Boudard, M. J. Carmezim and M. F. Montemor, *Sci. Rep.*, 2017, **7**, 39980–39990.
45 J. Liu, J. Wang, C. Xu, H. Jiang, C. Li, L. Zhang, J. Lin and Z. X. Shen, *Adv. Sci.*, 2018, **5**, 1700322–1700341.
46 J. Wang, J. Polleux, J. Lim and B. Dunn, *J. Phys. Chem. C*, 2007, **111**, 14925–14931.
47 J. Duay, S. A. Sherrill, Z. Gui, E. Gillette and S. B. Lee, *ACS Nano*, 2013, **7**, 1200–1214.
48 H. Tian, X. Yu, H. Shao, L. Dong, Y. Chen, X. Fang, C. Wang, W. Han and G. Wang, *Adv. Energy Mater.*, 2019, **9**, 1901560–1901572.
49 H. Zhou and H.-J. Zhai, *Org. Electron.*, 2016, **37**, 197–206.
50 R. Abazari, S. Sanati, A. Morsali, A. M. Z. Slawin, C. L. Carpenter-Warren, W. Chen and A. Zheng, *J. Mater. Chem. A*, 2019, **7**, 11953–11966.
51 P. Xu, T. Gu, Z. Cao, B. Wei, J. Yu, F. Li, J.-H. Byun, W. Lu, Q. Li and T.-W. Chou, *Adv. Energy Mater.*, 2014, **4**, 1300759–1300765.
52 W. Y. Ko, Y. F. Chen, K. M. Lu and K. J. Lin, *Sci. Rep.*, 2016, **6**, 18887–18894.
53 K. Qi, R. Hou, S. Zaman, Y. Qiu, B. Y. Xia and H. Duan, *ACS Appl. Mater. Interfaces*, 2018, **10**, 18021–18028.
54 S.-Y. Yang, Y.-F. Wang, Y. Yue and S.-W. Bian, *J. Electroanal. Chem.*, 2019, **847**, 113218–113227.
55 F. Su, X. Lv and M. Miao, *Small*, 2015, **11**, 854–861.
56 Z. Jiang, L. Sheng, Y. Lin, S. Zhang, L. Zhang, T. Wei, J. Zhou, C. Liu, H. Jiang, Q. Zhou and Z. Fan, *Chem. Eng. J.*, 2021, **426**, 131361–131371.
57 Z. Yang, Y. Yang, C.-x. Lu, Y.-y. Zhang, X.-h. Zhang and Y.-y. Liu, *New Carbon Mater.*, 2019, **34**, 559–568.
58 J.-h. Liu, X.-y. Xu, W. Lu, X. Xiong, X. Ouyang, C. Zhao, F. Wang, S.-y. Qin, J.-l. Hong, J.-n. Tang and D.-Z. Chen, *Electrochim. Acta*, 2018, **283**, 366–373.
59 W. Lyu, W. Zhang, H. Liu, Y. Liu, H. Zuo, C. Yan, C. F. J. Faul, A. Thomas, M. Zhu and Y. Liao, *Chem. Mater.*, 2020, **32**, 8276–8285.
60 X. Zheng, L. Yao, Y. Qiu, S. Wang and K. Zhang, *ACS Appl. Energy Mater.*, 2019, **2**, 4335–4344.
61 Y. Wu, Z. Meng, J. Yang and Y. Xue, *Nanotechnology*, 2021, **32**, 295401–295410.
62 Y. F. Wang, H. T. Wang, S. Y. Yang, Y. Yue and S. W. Bian, *ACS Appl. Mater. Interfaces*, 2019, **11**, 30384–30390.
63 C. Wei, Q. Xu, Z. Chen, W. Rao, L. Fan, Y. Yuan, Z. Bai and J. Xu, *Carbohydr. Polym.*, 2017, **169**, 50–57.
64 C. Zhou, M. Hong, Y. Yang, C. Yang, N. Hu, L. Zhang, Z. Yang and Y. Zhang, *J. Power Sources*, 2019, **438**, 227044–227054.
65 X. Pu, L. Li, M. Liu, C. Jiang, C. Du, Z. Zhao, W. Hu and Z. L. Wang, *Adv. Mater.*, 2016, **28**, 98–105.